Electronic Supplementary Information (ESI)

Defect-Driven Accelerated Structural Transformation from Metal-Organic Frameworks: A Boost for Oxygen Evolution Reaction

Han Wang,†[a] Dong Yan,†[a] Suran He,†[a] Tao Yu,[a] Fan Yang,[a] Mingxu Liu[a] and Chun-Chao Hou*[a]

[a] China-Australia Joint Research Center for Functional Molecular Materials, College of Materials Science and Engineering, Ocean University of China, Qingdao 266100, China.

† These authors contributed equally to this work.

Materials

Cobalt(II) nitrate hexahydrate ($Co(NO_3)_2 \cdot 6H_2O$, 98%), terephthalic acid (H_2BDC, 99%), 1,1'-ferrocene dicarboxylic acid (Fc, 98%), sodium hydroxide (NaOH, 97%), commercial ruthenium oxide (RuO_2, 99.9%), N, N-dimethylformamide (DMF) and ethanol are purchased from Aladdin (Shanghai, China). All reagents used in this study are of analytical grade and employed directly without further purification.

Catalysts preparation

Synthesis of CoFc-BDC/NF

The typical CoFc-BDC/NF is fabricated via a modified solvothermal method.[1] In this process, 0.15 mmol Fc and 0.85 mmol BDC are dissolved in 7.5 mL of DMF, followed by the addition of 1 mL 0.4 M NaOH under stirring. Meanwhile, 1 mmol $Co(NO_3)_2 \cdot 6H_2O$ is separately dissolved in 4.5 mL of DMF. The two solutions are combined and subsequently transferred into a Teflon-lined stainless-steel autoclave with a piece of NF (1.5 cm×3 cm) in it. After that, the autoclave is heated for 15 h at 100 °C. The resulting CoFc-BDC/NF is washed with DMF and ethanol three times and dried naturally. For convenience, unless otherwise stated, the optimized $CoFc_{0.15}$-$BDC_{0.85}$/NF is denoted as CoFc-BDC/NF.

Synthesis of $CoFc_{0.1}$-$BDC_{0.9}$/NF, $CoFc_{0.2}$-$BDC_{0.8}$/NF, and $CoFc_{0.3}$-$BDC_{0.7}$/NF

A similar method is adopted to synthesize various Co-based MOFs, except for varying the molar ratio of the ligand precursors (BDC and Fc) at the start. The total mole number of ligands is consistently maintained at 1 mmol. Based on the different ligands used, the final samples are correspondingly named as $CoFc_{0.1}$-$BDC_{0.9}$/NF, $CoFc_{0.2}$-$BDC_{0.8}$/NF, and $CoFc_{0.3}$-$BDC_{0.7}$/NF, respectively.

Synthesis of Co-BDC/NF

In this process, 1 mmol BDC is dissolved in 7.5 mL of DMF, followed by the addition of 1 mL 0.4 M NaOH under stirring. Meanwhile, 1 mmol $Co(NO_3)_2 \cdot 6H_2O$ is separately dissolved in 4.5 mL of DMF. The two solutions are combined and subsequently transferred into a Teflon-lined stainless-steel autoclave with a piece of NF (1.5 cm×3 cm) in it. After that, the autoclave is heated for 15 h at 100 °C. The resulting Co-BDC/NF is washed with DMF and ethanol three times and dried naturally.

Material characterizations

X-ray diffraction (XRD) pattern is obtained using a Bruker D8 Advance diffractometer operating at 40 kV and 40 mA, with Cu K_α radiation (λ = 1.54178 Å). Raman spectroscopy is performed with a Thermo Fisher spectrometer equipped with helium-neon (633 nm) and argon (532 nm) lasers. Scanning electron microscopy (SEM) images are measured with a Hitachi SU8010 system. Transmission electron microscopy (TEM) images are taken on a JEM-1400Plus TEM. Energy-dispersive X-ray spectroscopy (EDS) mapping images are recorded from a JEOL JEM-ARM200F

equipped with energy-dispersive X-ray spectrometer, operating at 200 kV. The X-ray photoelectron spectra (XPS) are recorded on the Thermo Scientific ESCALAB 250Xi spectrometer. All binding energies are calibrated to the C 1s peak at 284.8 eV, with a typical measurement uncertainty of ± 0.1 eV. Electron paramagnetic resonance (EPR) spectra are performed on Bruker EMX PLUS. The X-ray absorption fine structure spectra (XAS) are collected in transmission mode at room temperature.

Electrochemical measurements

Electrochemical measurements are performed using a CHI 760E electrochemical workstation with a conventional three-electrode setup in 1 M KOH at room temperature. The Ag/AgCl (3.5 M KCl) and platinum plate electrode are used as the reference and counter electrode respectively. All potentials reported versus the reversible hydrogen electrode (vs. RHE), using the following equation: E (vs. RHE) = E (vs. Ag/AgCl) + 0.197 + 0.0592 × pH. Linear sweep voltammetry (LSV) is conducted at a scan rate of 5 mV s^{-1}. The ohmic drop is corrected via the positive feedback method at a 95% compensation level, and all LSV curves are corrected for iR drop. The Tafel slope is determined by fitting the data to the Tafel equation [$\eta = b \log(j) + a$]. Electrochemical impedance spectroscopy (EIS) is performed over a frequency range of 10^5 to 0.01 Hz, with the potential set high enough to ensure OER occurrence. The double-layer capacitance (C_{dl}) is measured in a non-Faradaic region at various scan rates (v = 20, 40, 60, 80, and 100 mV·s^{-1}). Long-term stability tests are assessed via chronopotentiometry measurements at a current density of 100 mA·cm^{-2}.

AEM electrolyzer test

The anion exchange membrane water electrolyzer (AEMWE) is constructed with cathode and anode featuring a geometric active area of 1 cm^2, separated by an anion exchange membrane (FAA-3PK-130) with a thickness of 110-150 μm. The as-prepared CoFc-BDC/NF electrode serves as the anode catalyst, while the CoP/NF catalyst is employed as the cathode. The self-supported electrodes also function as the gas diffusion layers. The electrolyte is circulated through the AEM electrolyzer at a flow rate of 50 mL min^{-1} within a serpentine flow field. For comparative purposes, a control AEMWE cell is assembled with a Pt/C cathode and a NiFe-LDH@NF anode (active area: 1 cm^2). The gas back-pressure at the electrolyzer outlet is maintained at ambient atmospheric pressure. The overall water splitting performance of the AEM electrolyzer is evaluated using a CHI760E electrochemical workstation at 60 °C.

In-situ Raman

In-situ Raman spectra are recorded using the aforementioned confocal Raman microscope under 532 nm laser excitation, while electrochemical curves are collected using a CHI 760E electrochemical workstation. The electrolytic cell is fabricated from Teflon and equipped with a

thin round quartz glass plate as the cover to protect the microscope objective. The self-supported working electrodes are inserted through the wall of the cell to keep the plane of working electrode perpendicular to the incident laser. In the in-situ Raman test, the platinum sheet is used as a counter electrode, and the reference electrode is an Ag/AgCl electrode. Chronoamperometry (CA) measurement is performed at various potentials in 1 M KOH during the Raman measurement.

Computational method

The calculations are conducted using the Vienna Ab initio Software Package (VASP 5.4.4).[2] We employ a combination of the Perdew-Burke-Ernzerhof (PBE) projected gradient approximation and the projected augmented wave method within the framework of density functional theory (DFT).[3] The electron exchange correlation energy is determined using the PBE generalized gradient approximation (GGA).[4] A cutoff energy of 500 eV defines the plane wave basis set. To enhance the accuracy of the long-range van der Waals (vdW) interactions, we include a DFT-D3 correction based on the Grimme scheme.[5] Geometry optimization and electronic structure calculations utilize a 3 × 3 × 1 Monkhorst-Pack special k-point grid. During optimization, atoms are allowed to relax freely, with maximum force and energy convergence thresholds set at 0.02 eV/Å and 1×10^{-5} eV/atom, respectively. Additionally, a 15 Å vacuum layer is introduced to eliminate interactions between periodic images. Furthermore, the free energy of the intermediates is determined by the following equation:

$$\Delta G = \Delta E + \Delta ZPE + \Delta U (0 \rightarrow T) - T\Delta S$$

In the aforementioned equation, ΔE represents the total energy obtained from DFT calculations; ΔZPE denotes the change in zero-point energy, acquired from vibrational frequency calculations; TΔS indicates the entropic contribution at a specified temperature T (typically 298.15 K), derived from vibrational analysis. ΔU (0 → T) serves as a correction term for the ground-state energy, accounting for the energy increase of the system due to heating to temperature T. For the Oxygen Evolution Reaction (OER) as a canonical example, the Gibbs free energy for each elementary step (e.g., $*OH \rightarrow *O + H^+ + e^-$) is calculated at U=0 V vs. RHE.

We leverage VASPKIT for these pertinent data modifications.[6]

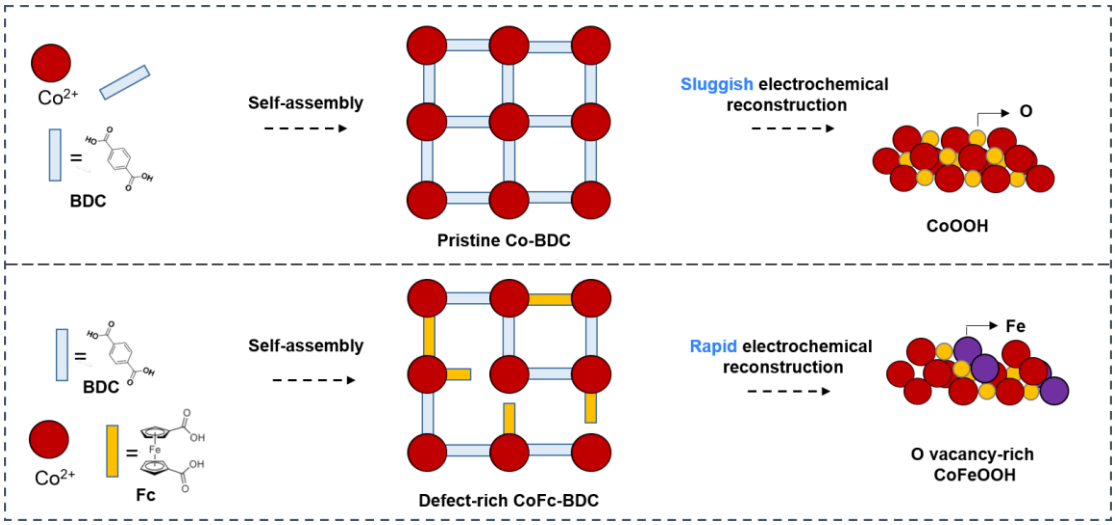

Figure S1. Schematic illustration of synthesis and reconstruction processes of CoFc-BDC and Co-BDC.

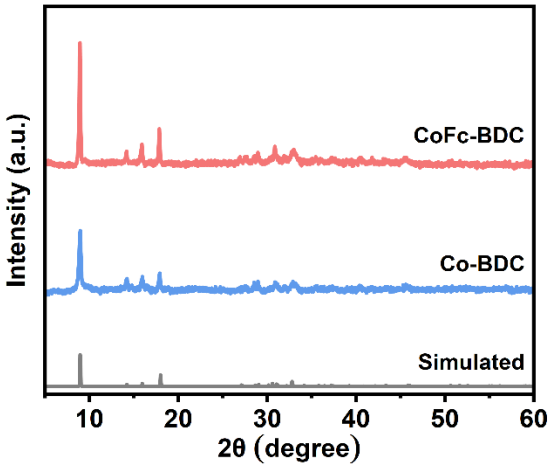

Figure S2. XRD patterns of CoFc-BDC and Co-BDC.

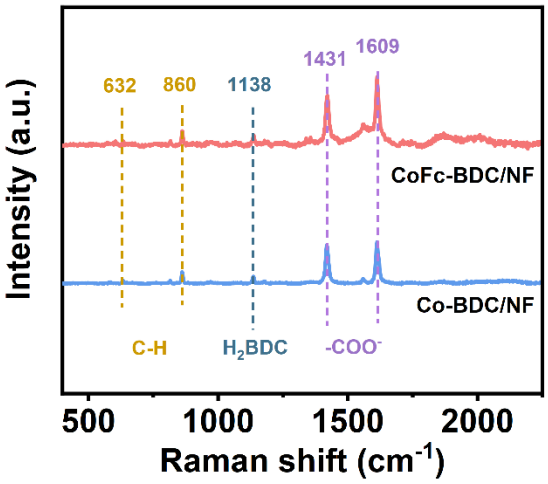

Figure S3. Raman spectra of CoFc-BDC/NF and Co-BDC/NF.

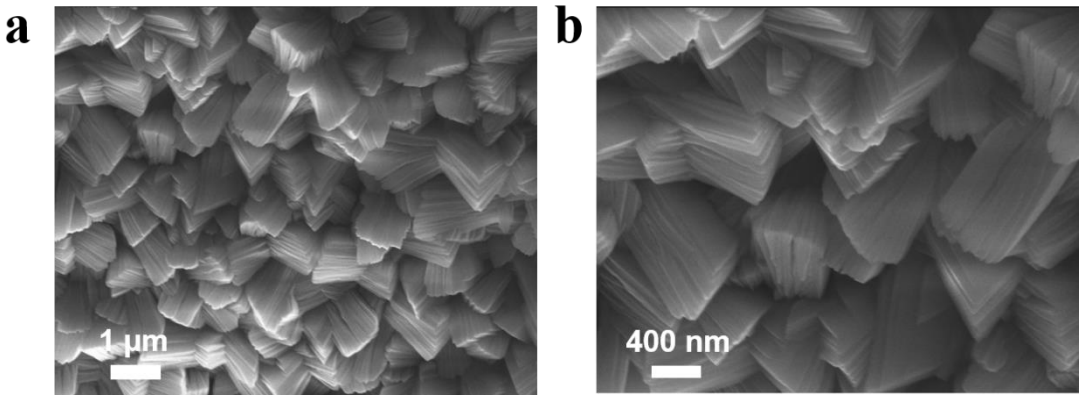

Figure S4. SEM images of Co-BDC/NF.

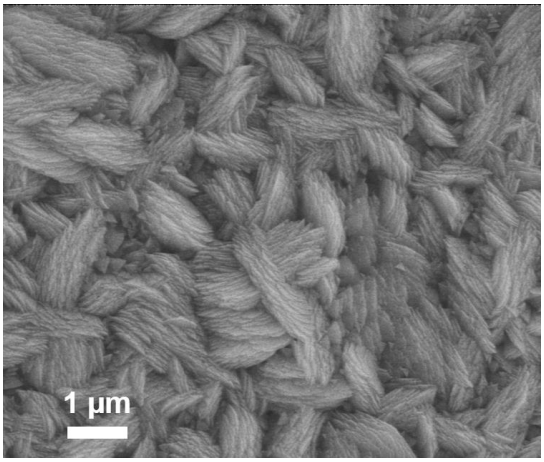

Figure S5. SEM image of CoFc-BDC/NF.

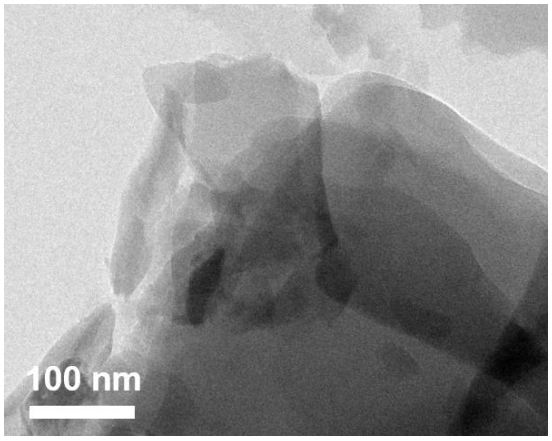

Figure S6. TEM image of Co-BDC.

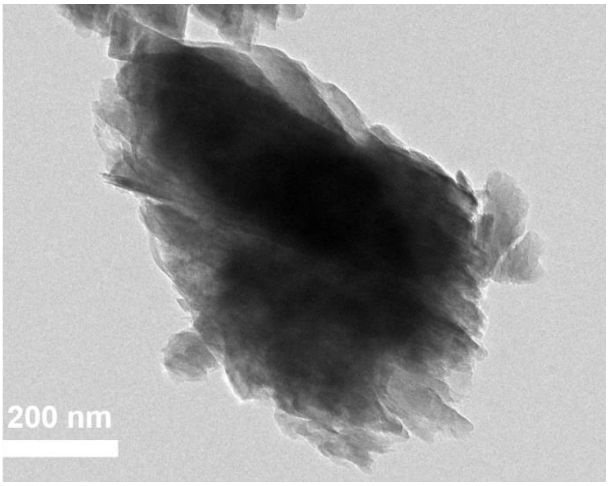

Figure S7. TEM image of CoFc-BDC.

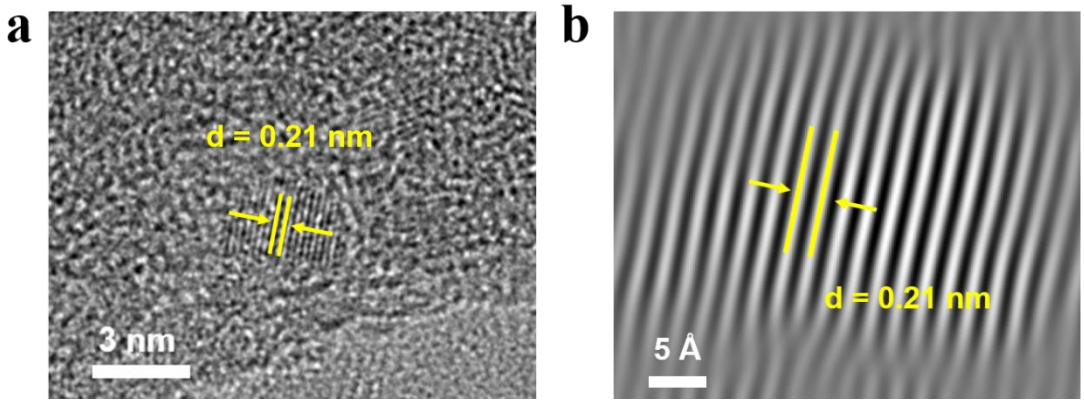

Figure S8. (a) HR-TEM image and (b) corresponding IFFT pattern of lattice fringes for Co-BDC.

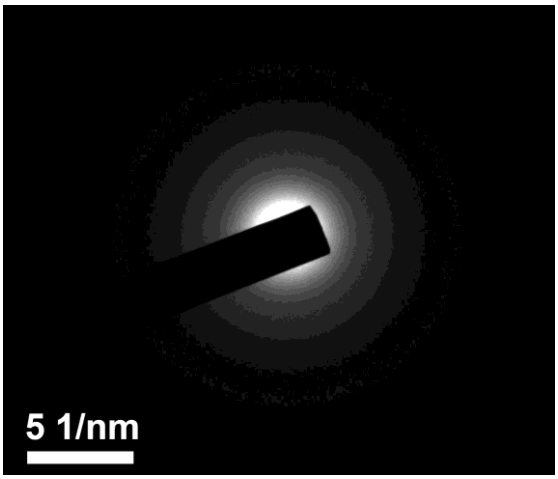

Figure S9. SAED pattern of CoFc-BDC.

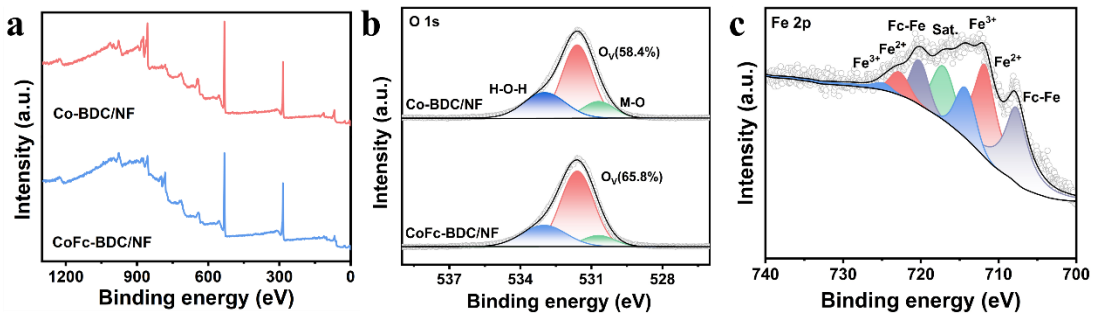

Figure S10. (a) XPS survey. High-resolution (b) O 1s and (c) Fe 2p spectra of Co-BDC/NF and CoFc-BDC/NF, respectively.

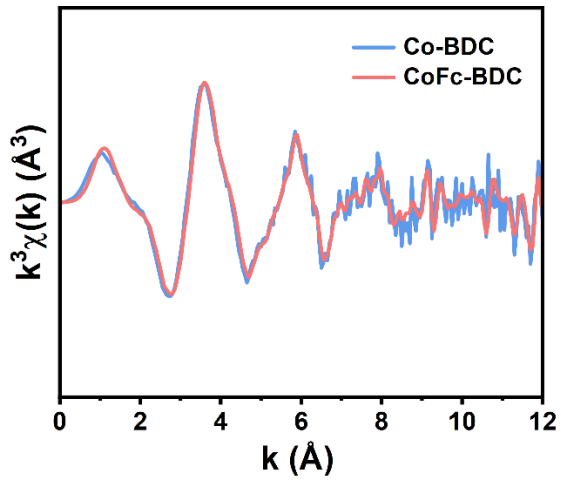

Figure S11. Co K-edge EXAFS of oscillations for Co-BDC and CoFc-BDC.

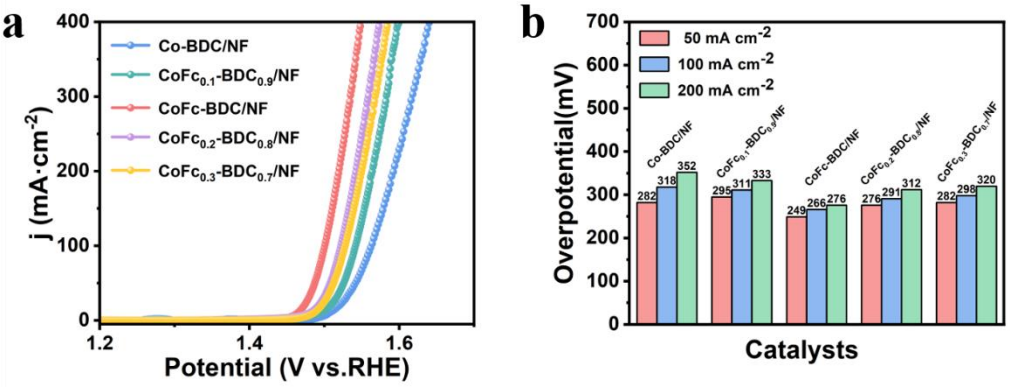

Figure S12. (a) LSV curves and (b) the overpotential comparison of as-prepared catalysts.

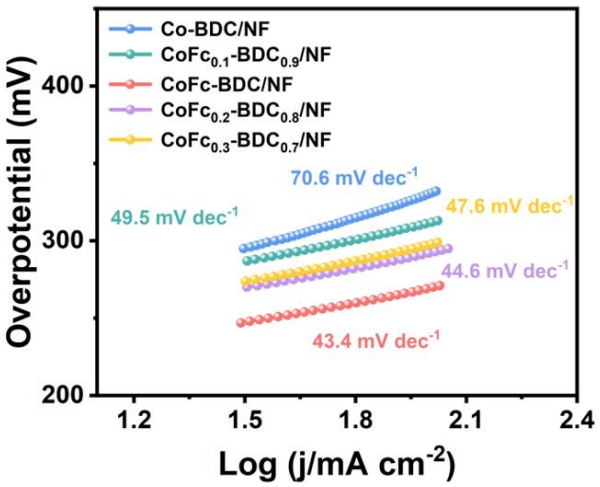

Figure S13. Tafel slopes of as-prepared catalysts.

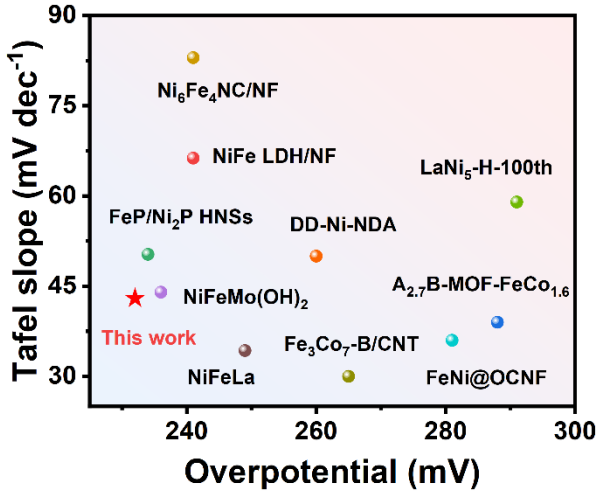

Figure S14. The comparison of the overpotential at 10 mA cm^{-2} and Tafel slope with previously reported catalysts.

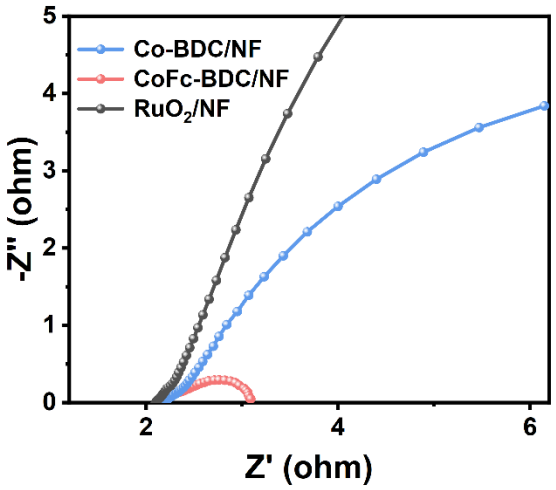

Figure S15. Nyquist plots of CoFc-BDC/NF, Co-BDC/NF, and commercial RuO_2/NF.

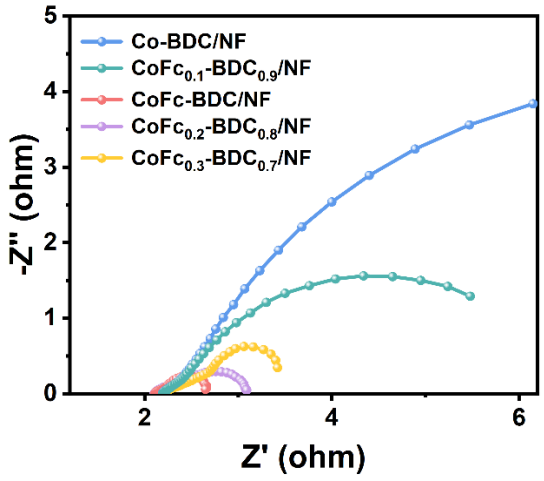

Figure S16. The EIS plots of as-prepared catalysts.

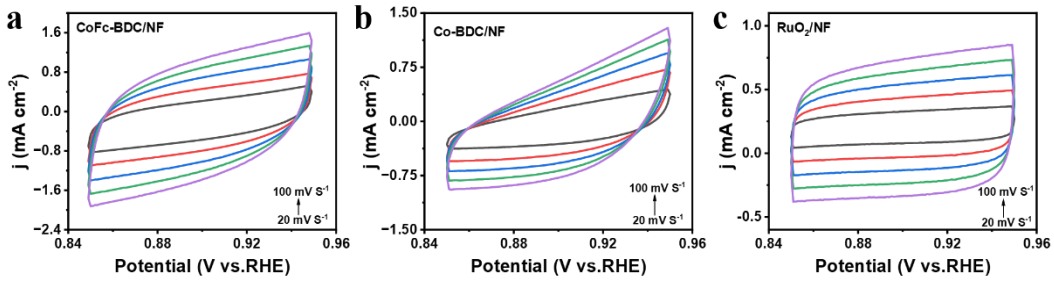

Figure S17. CV curves of (a) CoFc-BDC/NF, (b) Co-BDC/NF and (c) RuO_2/NF in 1 M KOH.

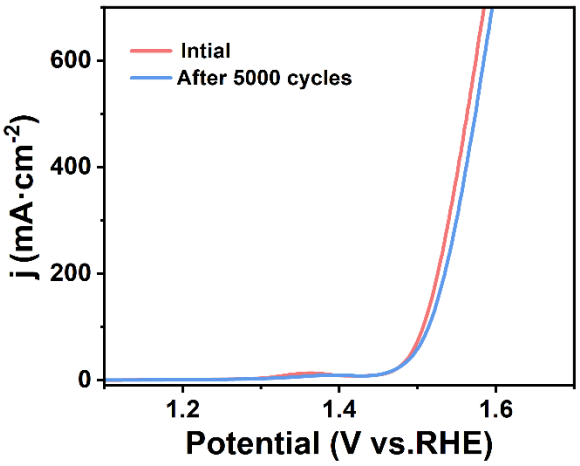

Figure S18. The LSV curves of CoFc-BDC/NF before and after 5000 cycles.

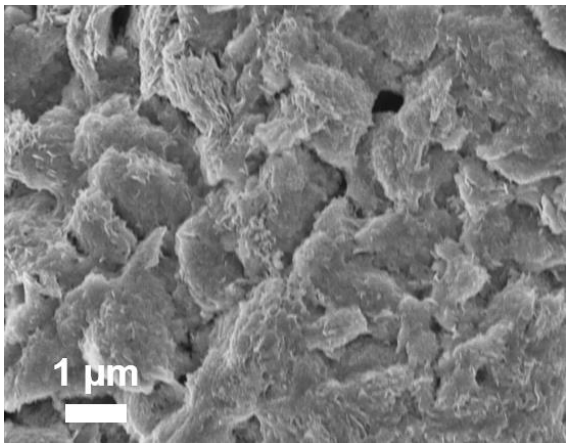

Figure S19. SEM image of CoFc-BDC/NF after the OER test.

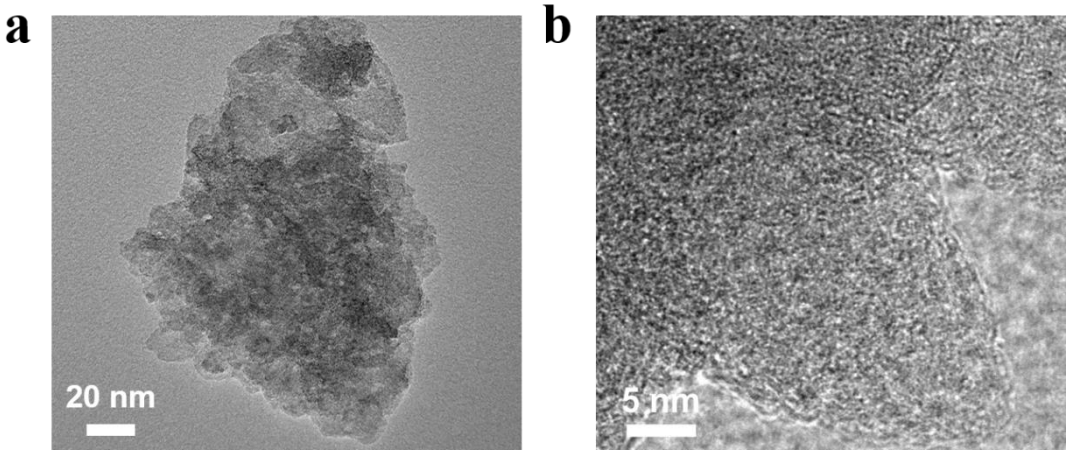

Figure S20. (a) TEM image and (b) HR-TEM image of CoFc-BDC after the OER test.

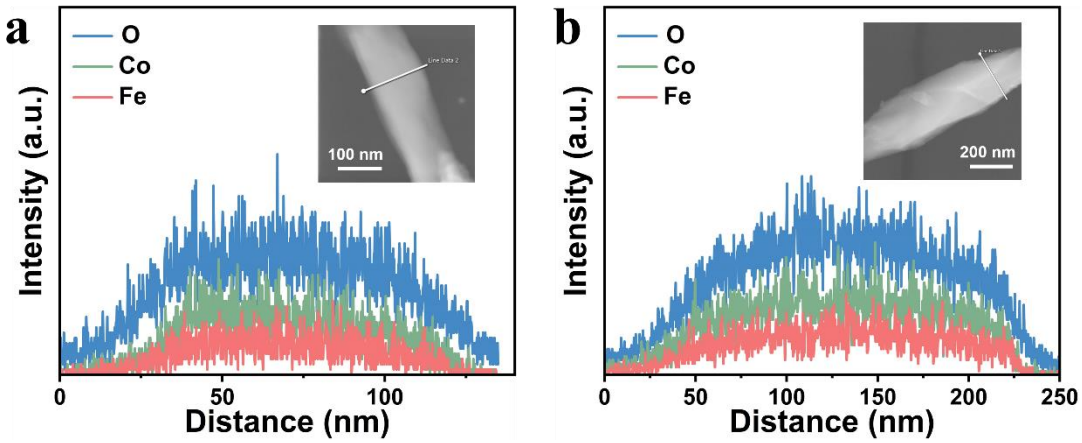

Figure S21. Elemental line-scan analysis of CoFc-BDC (a) before and (b) after the OER test.

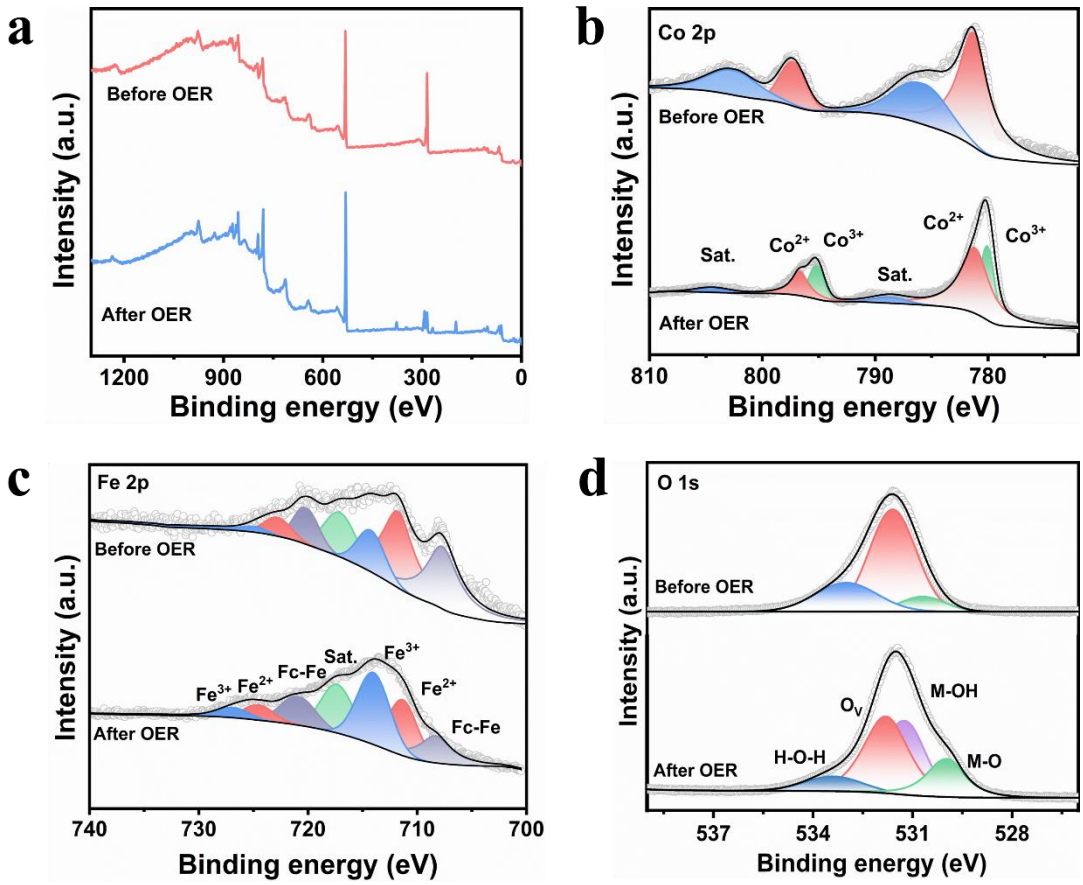

Figure S22. (a) XPS survey. High-resolution (b) Co 2p, (c) Fe 2p, and (d) O 1s spectra of CoFc-BDC/NF before and after the OER test.

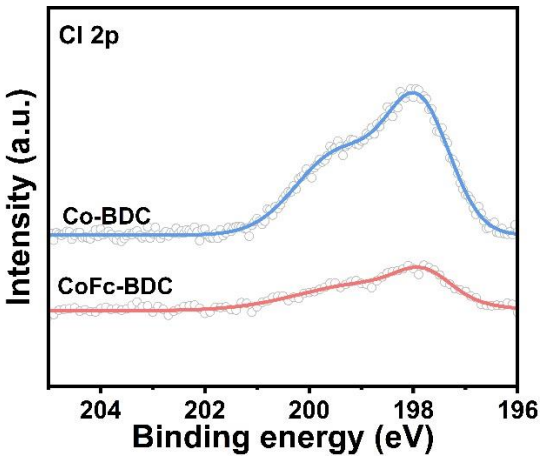

Figure S23. XPS Cl 2p spectra of Co-BDC and CoFc-BDC after the OER test in alkaline seawater.

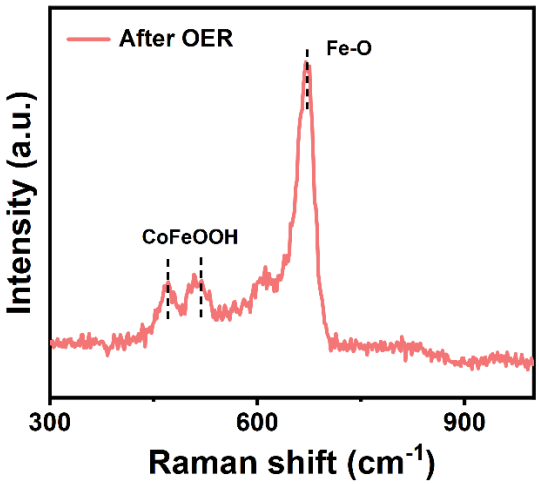

Figure S24. Raman spectra of CoFc-BDC/NF after the OER test.

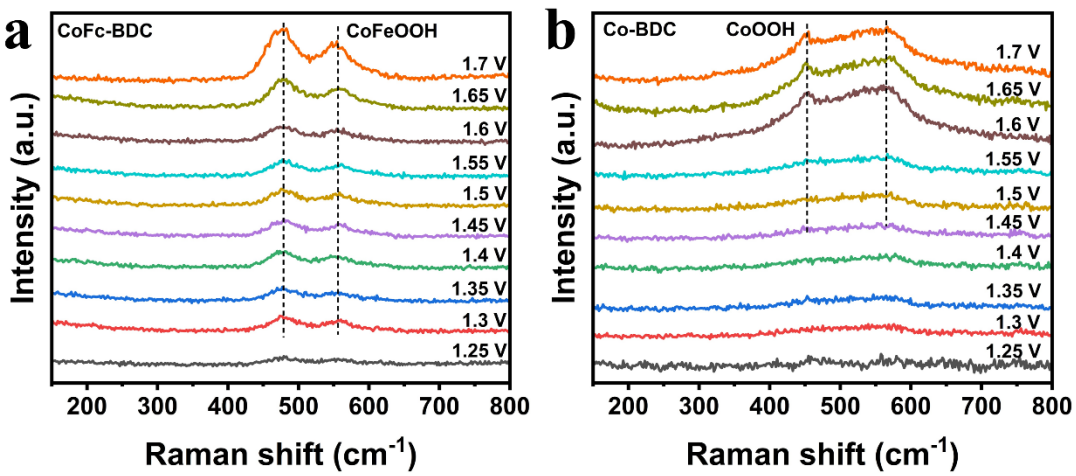

Figure S25. In situ Raman spectra of (a) CoFc-BDC and (b) Co-BDC.

As shown in Figure S25, when a high potential is applied, two characteristic peaks appear at 473 cm^{-1} and 551 cm^{-1} in the Raman spectrum of CoFc-BDC, and these signals correspond to the formation of CoFeOOH species during the oxidation process. Compared with Co-BDC, the Raman characteristic peaks of CoFc-BDC emerge at a lower potential and gradually intensify with the increase of potential, indicating that the introduction of defective ligands enables CoFc-BDC to undergo structural transformation at a reduced potential and accelerates the catalyst reconstruction process. The CoFeOOH layer formed by rapid self-reconstruction can block the corrosion of the electrode by chloride ions. Moreover, under the operating potential, the negatively charged oxygen-containing species on the surface of CoFeOOH exert electrostatic repulsion on the also negatively charged Cl^- ions, making it difficult for Cl^- to approach the catalytic active sites and thus inhibiting the adsorption of Cl^- and the subsequent chlorine evolution reaction (CER).

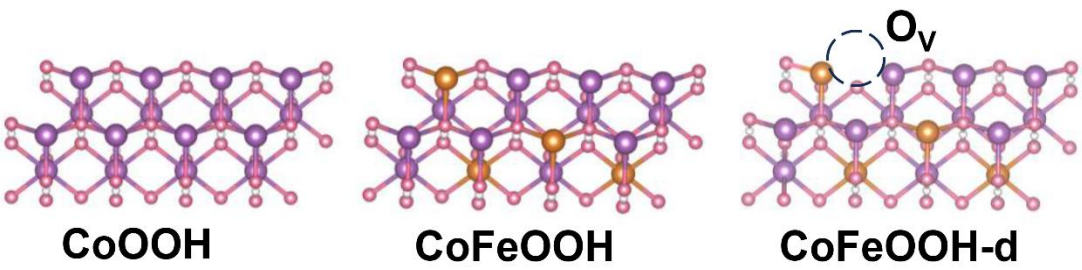

Figure S26. The structural model of CoOOH, CoFeOOH and CoFeOOH-d.

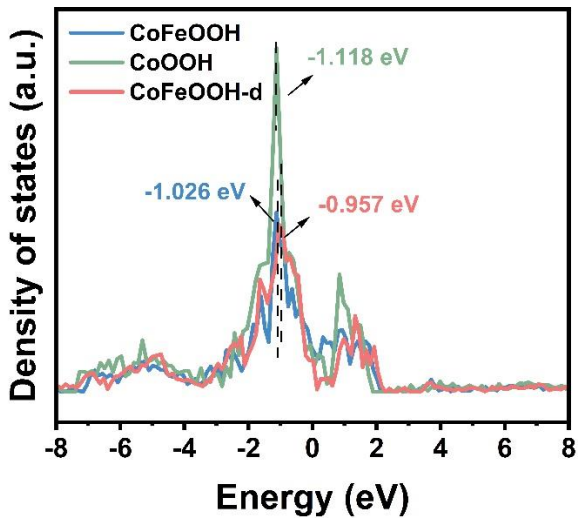

Figure S27. PDOS calculated for CoOOH, CoFeOOH and CoFeOOH-d.

As shown in Figure S27, compared with the d-band center of CoOOH at -1.118 eV, that of CoFeOOH is upshifted to -1.026 eV, indicating that the introduction of Fe induces significant charge rearrangement. For CoFeOOH-d with oxygen vacancies, its d-band center is further upshifted to -0.957 eV. These results confirm that oxygen vacancies can activate the surrounding metal active sites and optimize their adsorption capacity for reaction intermediates.

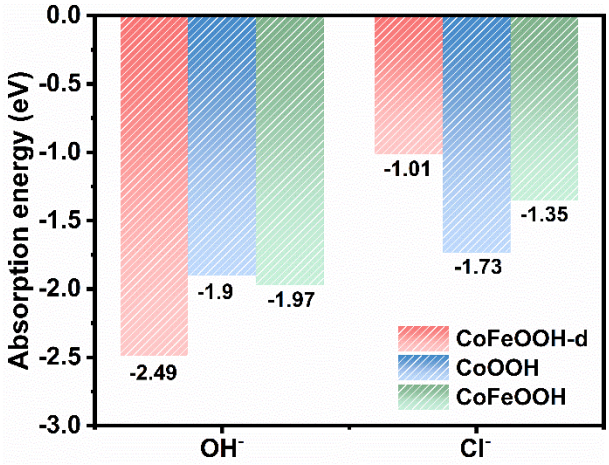

Figure S28. The adsorption energy of Cl^- and OH^- on CoOOH, CoFeOOH and CoFeOOH-d, respectively.

As shown in Figure 28, the adsorption energy of OH^- on the CoFeOOH-d surface is -2.49 eV, while that of Cl^- is only -1.01 eV, indicating that the adsorption strength of OH^- is significantly stronger than that of Cl^-. These results demonstrate that the active surface of the catalyst exhibits an intrinsic and thermodynamically stronger adsorption preference for the OH^-. Such a prominent preference enables OH^- to competitively and fully occupy all active sites during the reaction process, thereby significantly kinetically inhibiting the adsorption of Cl^- and its subsequent oxidative corrosion reaction.

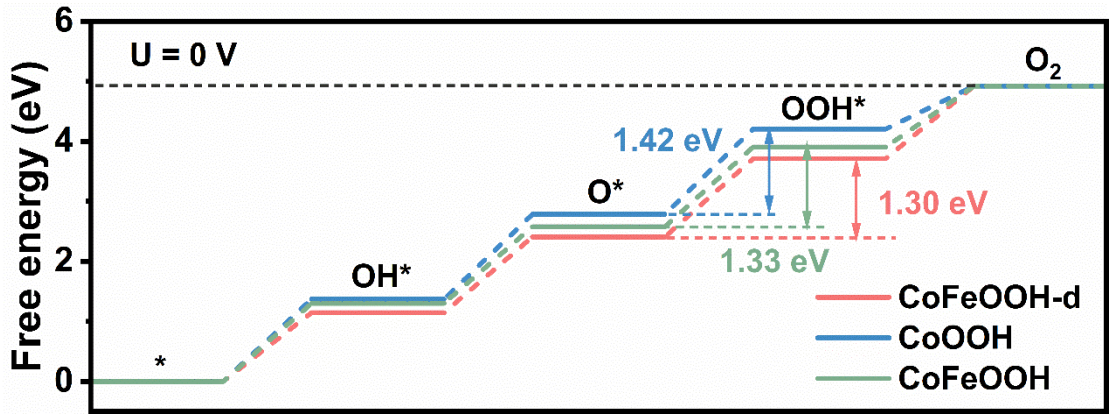

Figure S29. The reaction energy change of OER under U = 0 V.

As shown in Figure S29, the Gibbs free energy of each elementary step along the adsorbate evolution mechanism (AEM) pathway on the catalyst surface reveals that the rate-determining step (RDS) of all three structures is the *O → *OOH step. The RDS energy barrier of CoOOH is 1.42 eV, whereas the incorporation of Fe reduces the energy barrier of this key step to 1.33 eV in CoFeOOH, indicating that the introduction of Fe can significantly lower the OER RDS energy barrier. Furthermore, the RDS energy barrier of CoFeOOH-d is further reduced, confirming that oxygen vacancies regulate the local electronic structure and optimize the adsorption free energy of adjacent Co sites for oxygen-containing intermediates, thereby accelerating the reaction process.

Table S1. Comparison of the OER activities of previously reported electrocatalysts.

Sample	η (mV) @10 mA cm^{-2}	Tafel slope ($mV\ dec^{-1}$)	Reference
CoFc-BDC/NF	232	43	This work
$NiFeMo(OH)_2$	236	44	[7]
NiFe LDH/NF	241	66.3	[8]
$A_{2.7}B$-MOF-$FeCo_{1.6}$	288	39	[9]
FeP/Ni_2P HNSs	234	50.3	[10]
Ni_6Fe_4NC/NF	241	83	[11]
FeNi@OCNF	281	36	[12]
NiFeLa	249	34.3	[13]
Fe_3Co_7-B/CNT	265	30	[14]
DD-Ni-NDA	260	50	[15]
$LaNi_5$-H-100th	291	59	[16]
CoCrV LTH	290	39	[17]
Ni_8Co_2-BDC	274	73.1	[18]
CoZn MOF/CC	287	76.3	[19]
NiPc-$NiFe_{0.09}$	300	55	[20]

References

1 Z. Xue, K. Liu, Q. Liu, Y. Li, M. Li, C. Su, N. Ogiwara, H. Kobayashi, H. Kitagawa, M. Liu and G. Li, *Nat Commun.*, 2019, **10**, 5048

2 G. Kresse and J. Furthmüller, *Comput. Mater. Sci.,* 1996, **6**, 15-50.

3 P. E. Blöchl, *Phys. Rev. B,* 1994, **50**, 17953-17979.

4 J. P. Perdew, K. Burke and M. Ernzerhof, *Phys. Rev. Lett.*, 1996, **77**, 3865-3868.

5 S. Grimme, J. Antony, S. Ehrlich and H. Krieg, *J. Chem. Phys.,* 2010, **132**, 154104.

6 V. Wang, N. Xu, J.-C. Liu, G. Tang and W.-T. Geng, *Comput. Phys. Commun.*, 2021, **267**, 108033.

7 J. Wang, Z. Xing, R. Kang, Y. Zheng, Z. Zhang, T. Ma, Y. Wang, B. Yin, Y. Liao, L. Li, C. Cheng and S. Li, *Adv. Funct. Mater.*, 2025, **35**, 2418439.

8 F. Li, S. Xu, X. Zhao, G. Ma, Z. Niu, X. Zhong and J. Li, *Small,* 2025, **21**, 2304260.

9 Z. Xue, Y. Li, Y. Zhang, W. Geng, B. Jia, J. Tang, S. Bao, H.-P. Wang, Y. Fan, Z.-w. Wei, Z. Zhang, Z. Ke, G. Li and C.-Y. Su, *Adv. Energy Mater.*, 2018, **8**, 1801564.

10 Y. Feng, C. Xu, E. Hu, B. Xia, J. Ning, C. Zheng, Y. Zhong, Z. Zhang and Y. Hu, *J. Mater. Chem. A*, 2018, **6**, 14103-14111.

11 D. Thiruvengadam, K. Umapathy, M. Muthamildevi, A. Gayathri, B. Vishnu and J. Jayabharathi, *Energy & Fuels*, 2024, **38**, 21095-21108.

12 P. He, Y. Wu, H. Chen, Z. Zhu, H. Liu, J. Gao and H. Xu, *J. Alloy. Compd.*, 2020, **813**, 152192.

13 X. Wang, W. Pi, S. Hu, H. Bao, N. Yao and W. Luo, *Nanomicro Lett.*, 2024, **17**, 11.

14 J.M.V. Nsanzimana, L. Gong, R. Dangol, V. Reddu, V. Jose, B.Y. Xia, Q. Yan, J.-M. Lee and X. Wang, *Adv. Energy Mater.*, 2019, **9**, 1901503.

15 Y. Liu, X. Li, S. Zhang, Z. Wang, Q. Wang, Y. He, W. Huang, Q. Sun, X. Zhong, J. Hu, X. Guo, Q. Lin, Z. Li, Y. Zhu, C. Chueh, C. Chen, Z. Xu and Z. Zhu, *Adv. Mater.,* 2023, **35**, 2300945.

16 Z. Chen, H. Yang, S. Mebs, H. Dau, M. Driess, Z. Wang, Z. Kang and P. Menezes, *Adv. Mater.*, 2023, **35**, 2208337.

17 S. Khatun and P. Roy, *Chem. Commun.*, 2022, **58**, 1104-1107.

18 J. Zhou, F. Qiao, Z. Ren, X. Hou, Z. Chen, S. Dai, G. Su, Z. Cao, H. Jiang and M. Huang, *Adv. Funct. Mater.*, 2024, **34**, 2304380.

19 J. Wu, Z. Yu, Y. Zhang, S. Niu, J. Zhao, S. Li and P. Xu, *Small*, 2021, **17**, 2105150.

20 J. Li, P. Liu, J. Mao, J. Yan and W. Song, *J. Mater. Chem. A*, 2021, **9**, 11248-11254.